

LETTER TO THE EDITOR

# Detection of an excessively strong 3- $\mu\text{m}$ absorption near the lunar highland crater Dufay

C. Wöhler<sup>1</sup>, A. Grumpe<sup>1</sup>, M. Bhatt<sup>2</sup>, A. A. Berezhnoy<sup>3</sup>, V. V. Shevchenko<sup>3</sup>, and A. Bhardwaj<sup>2</sup>

<sup>1</sup> Image Analysis Group, TU Dortmund University, Otto-Hahn-Str. 4, 44227 Dortmund, Germany

e-mail: christian.woehler@tu-dortmund.de

<sup>2</sup> Physical Research Laboratory, Ahmedabad 380009, India

e-mail: megha@prl.res.in

<sup>3</sup> Sternberg Astronomical Institute, Moscow State University, Universitetskij Pr., 13, 119234 Moscow, Russia

e-mail: a\_tolok@mail.ru

Received 20 May 2019 / Accepted 6 September 2019

## ABSTRACT

Using the near-infrared spectral reflectance data of the Chandrayaan-1 Moon Mineralogy Mapper ( $M^3$ ) instrument, we report an unusually bright structure of  $30 \times 60 \text{ km}^2$  on the lunar equatorial farside near crater Dufay. At this location, the 3- $\mu\text{m}$  absorption band feature, which is commonly ascribed to hydroxyl (OH) and/or water ( $\text{H}_2\text{O}$ ), at local midday is significantly ( $\sim 30\%$ ) stronger than on the surrounding surface and, surprisingly, stronger than in the illuminated polar highlands. We did not find a similar area of excessively strong 3- $\mu\text{m}$  absorption anywhere else on the Moon. A possible explanation for this structure is the recent infall of meteoritic or cometary material of high OH/ $\text{H}_2\text{O}$  content forming a thin layer detectable by its pronounced 3- $\mu\text{m}$  band, where a small amount of the OH/ $\text{H}_2\text{O}$  is adsorbed by the surface material into binding states of relatively high activation energy. Detailed analysis of this structure with next-generation spacecraft instrumentation will provide further insight into the processes that lead to the accumulation of OH/ $\text{H}_2\text{O}$  in the lunar regolith surface.

**Key words.** Moon – planets and satellites: surfaces – planets and satellites: composition – infrared: planetary systems – solid state: volatile

## 1. Introduction

The occurrence of hydroxyl (OH) and/or water ( $\text{H}_2\text{O}$ ) on the surface of the Moon has been shown based on orbital near-infrared (NIR) hyperspectral image data acquired by the Moon Mineralogy Mapper ( $M^3$ ) instrument (Pieters et al. 2009a) on the spacecraft Chandrayaan-1 (Goswami & Annadurai 2009), revealing an absorption band at wavelengths around 2.8–3.0  $\mu\text{m}$  (Pieters et al. 2009b). The analysis of NIR reflectance spectra of the lunar surface furthermore led to the identification of time-of-day-dependent variations of the 3- $\mu\text{m}$  band depth (Sunshine et al. 2009; Li & Milliken 2017; Wöhler et al. 2017a,b). A commonly accepted explanation of the existence of lunar surficial OH/ $\text{H}_2\text{O}$  is the reaction between adsorbed protons from the solar wind with oxygen atoms contained in the surface material (e.g., Starukhina 2001; Farrell et al. 2015, 2017; Grumpe et al. 2019).

Localized anomalies of the 3- $\mu\text{m}$  band depth were found at lunar swirls, bright irregular structures associated with local magnetic fields (e.g., Tsunakawa et al. 2015), where the 3- $\mu\text{m}$  band is less pronounced than on the surrounding surface (Kramer et al. 2011; Bhardwaj et al. 2015; Grumpe et al. 2017; Li & Milliken 2017). A common explanation for this behavior is magnetic shielding of the surface from solar wind protons (e.g., Kramer et al. 2011). In the lunar highlands, localized areas of increased 3- $\mu\text{m}$  band depth have been observed in  $M^3$  data of regions known for their ancient volcanic activity (Bhattacharya et al. 2013), but those results were presumably obtained based on the thermal-emission-removal approach by Clark et al. (2011),

which is meanwhile known to systematically underestimate the surface temperature for some terrain types (e.g., Bandfield et al. 2016, 2018; Li & Milliken 2016); see Sect. 2. These positive 3- $\mu\text{m}$  band depth anomalies could not be reproduced when using a physically based method for thermal-emission removal (Wöhler et al. 2017b).

In this study, we describe based on the analysis of  $M^3$  data the detection of a strong localized positive 3- $\mu\text{m}$  band depth anomaly centered at  $170.5^\circ \text{ E}$  and  $8^\circ \text{ N}$  (Figs. 1a and b) and associated with a bright structure of about  $30 \times 60 \text{ km}^2$  size elongated in southeastern-northwestern direction (Fig. 1c). This unique structure is situated immediately southwest of the farside highland crater Dufay, half-way to the crater Dufay X (Figs. 1a and b). It does not have any perceivable topographic expression. Notably, the floor of Dufay X exhibits a swirl associated with a small localized magnetic anomaly (Denevi et al. 2016) (Fig. A.1). A region elongated in the north-south direction showing a similarly deep 3- $\mu\text{m}$  band appears in the southeastern lunar farside (Fig. A.2) approximately along the  $225^\circ \text{ E}$  meridian, but it is restricted to a single  $M^3$  strip and thus likely corresponds to a calibration artifact not considered for further study.

## 2. Data and methods

The 3- $\mu\text{m}$  band depth is strongly influenced by the thermal emission of the surface, which needs to be corrected for. The specific method used for thermal-emission removal has a strong

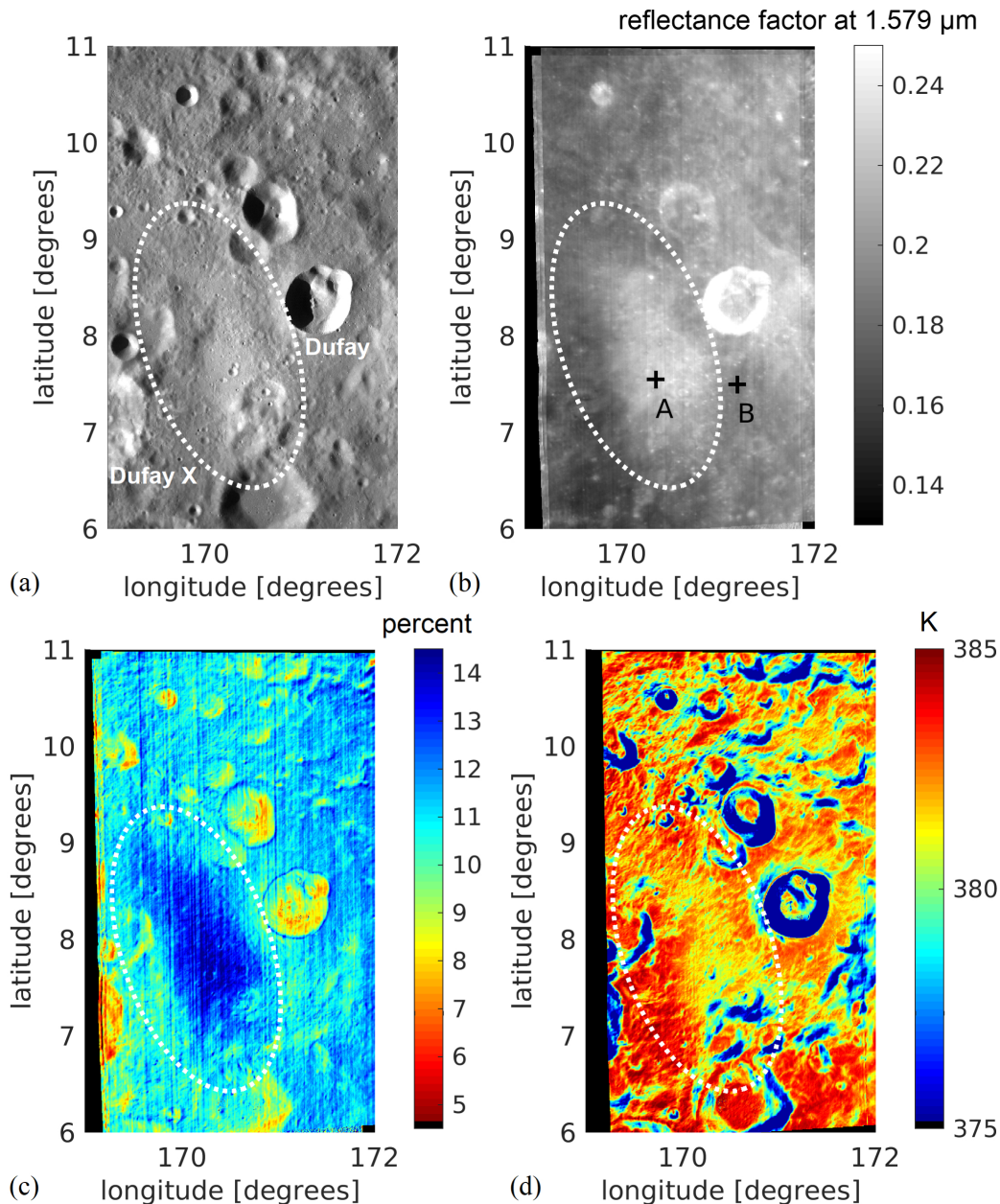


**Fig. 1.** Bright structure southwest of the crater Dufay (marked by white dashed oval). Black pixels denote missing data. *Panel a:* mosaic of Lunar Reconnaissance Orbiter (LRO) Wide Angle Camera (WAC) data (Speyerer et al. 2016; Sato et al. 2014). *Panel b:*  $M^3$  reflectance at  $1.579\ \mu\text{m}$ . Crosses indicate the locations of the spectra shown in Fig. 2. *Panel c:*  $3\text{-}\mu\text{m}$  band depth at midday (average of 10:00 and 11:45 data). *Panel d:* map of the effective temperature at 11:45.

influenced on the perceived properties of the  $3\text{-}\mu\text{m}$  absorption band. It is commonly known (e.g., Bandfield et al. 2016, 2018; Li & Milliken 2016) that the surface temperature provided by the “official”  $M^3$  level-2 data processing framework (Isaacson et al. 2011; Clark et al. 2011) is systematically underestimated. Our analysis is therefore based on the  $M^3$  level-1B spectral radiance images available on the Planetary Data System (PDS). We applied our previously described method for thermal-emission removal (Wöhler et al. 2017a,b; Grumpe et al. 2019), which is based on the Hapke model (Hapke 1984, 2002) and on the thermal equilibrium approach of Shkuratov et al. (2011), to model simultaneously the temperature, spectral emissivity, and bidirectional spectral reflectance of the surface. An initial estimate of the surface temperature is obtained by fitting the superposition of a reference reflectance spectrum linearly

extrapolated to the  $3\text{-}\mu\text{m}$  range and a black-body emission spectrum to the observed  $M^3$  reflectance spectrum. An iterative scheme is then applied to subsequently refine the bidirectional spectral reflectance, the spectral emissivity, and the surface temperature, which are all mutually interdependent. The iteration proceeds until the estimated temperature changes by less than 0.01 K between two iterations.

A significant influence on the surface temperature is exerted by the small-scale surface roughness (Bandfield et al. 2015; Davidsson et al. 2015). We assume that the rough surface is composed of small facets, each of which is characterized by an individual solar incidence angle and thus an individual temperature and thermal emission spectrum. The thermal emission of the rough surface can then be taken to correspond to the sum of the thermal emission spectra of all surface facets. As a consequence,

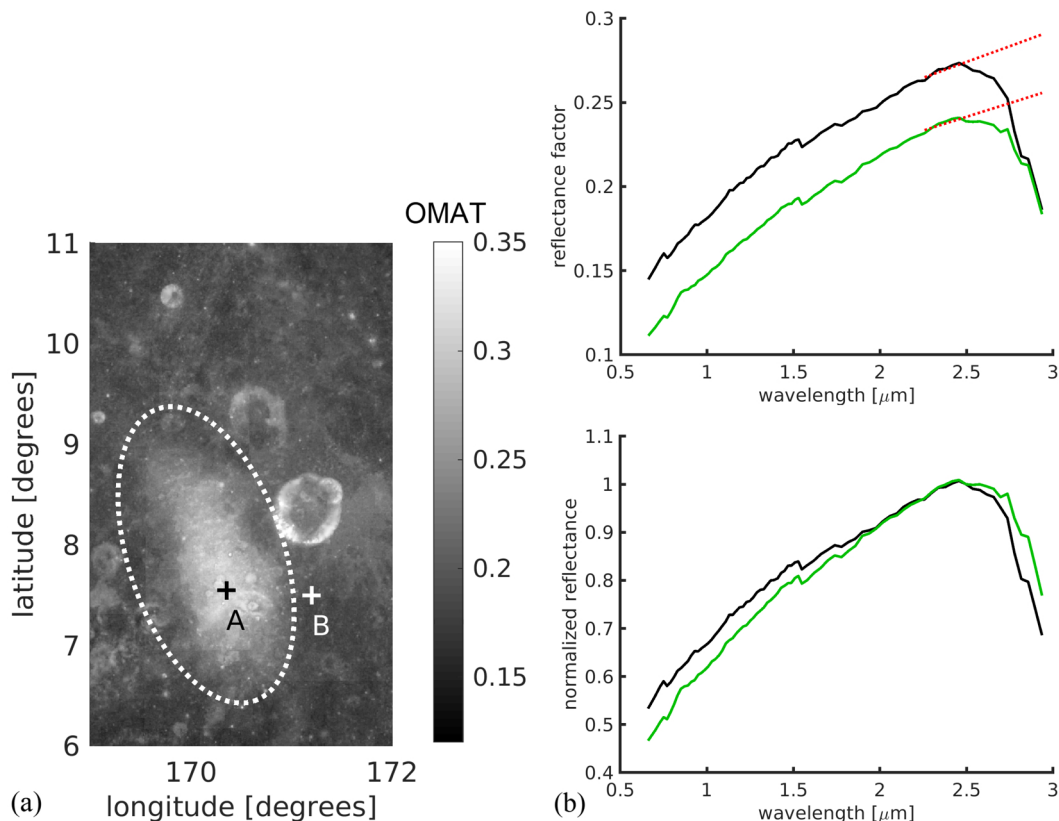


**Fig. 2.** *Panel a:* map of the Clementine-derived OMAT parameter as given by Lucey et al. (2000). Small “holes” due to invalid pixels were filled by interpolation. *Panel b:* spectrum of the bright structure (black curve) in comparison to the surrounding surface (green curve), averaged over  $1 \times 1 \text{ km}^2$  areas at the locations A and B indicated in Fig. 1b. The spectra were obtained by fitting the Hapke model (Hapke 1984, 2002) to the two available  $M^3$  images. *Top:* absolute reflectance factor. The dotted lines correspond to the fitted linear continuum. *Bottom:* reflectance normalized at  $2.5 \mu\text{m}$  (*bottom*).

the thermal emission of the surface is not consistent with one single temperature value. However, across the wavelength range up to  $3 \mu\text{m}$  it is a good approximation to replace the sum of the facet-specific thermal emission spectra by a single black-body spectrum of an effective temperature (Wöhler et al. 2017a). We used the calibration table of Wöhler et al. (2017a), who inferred a correction of the temperature of a smooth surface for a broad range of incidence angles and degrees of surface roughness. In this study we assumed a surface with a root-mean-square slope angle of  $9^\circ$ . It has been shown (Wöhler et al. 2017b; Grumpe et al. 2019) that the  $3\text{-}\mu\text{m}$  band depth remains qualitatively similar when a value of  $20^\circ$  as proposed by Bandfield et al. (2018) is used instead, which is due to the weak influence of the surface roughness on the thermal emission at low incidence angles (Bandfield et al. 2015; Grumpe et al. 2019), as is the case here. A detailed analysis of the range of surface roughness values to be used for thermal-emission removal was conducted by Grumpe et al. (2019).

Notably, both correcting the spectral radiance for thermal emission and normalizing the  $M^3$  bidirectional spectral reflectance to a uniform illumination and observation geometry requires a topographic map of the region under study of the same resolution as the  $M^3$  images used. For this purpose, we applied the photoclinometry-based technique of Grumpe & Wöhler (2014), where the GLD100 topographic map (Scholten et al. 2012) serves as a reference on large spatial scales. To all  $M^3$  level-1B spectral radiance measurements available for a specific image location, a unique value of the single-scattering albedo as defined by the Hapke model (Hapke 1984, 2002) is fit-

ted, which is then inserted into the Hapke model using uniform values of  $30^\circ$  incidence angle and  $0^\circ$  emission angle (Isaacson et al. 2011) for each  $M^3$  channel. The other parameters of the model of Hapke (1984, 2002) are taken from the first global lunar parameter set derived by Warell (2004). For details see Grumpe & Wöhler (2014) and also Wöhler et al. (2014).

Isaacson et al. (2013) suggested the application of a so-called “ground truth correction” to the  $M^3$  data, which aims at recovering shapes of the  $1\text{-}\mu\text{m}$  absorption band that are similar to those found for mature lunar soils. However, since this correction was designed such that it does not change the reflectance spectrum for wavelengths beyond  $2.5 \mu\text{m}$  (Isaacson et al. 2013), we have not used it in this study. We have also not used the “statistical polishing” algorithm described by Isaacson et al. (2011).

Laboratory measurements of the  $3\text{-}\mu\text{m}$  band shape in terrestrial (Dyar et al. 2010; Milliken 2006) and meteoritic (Beck et al. 2010; Takir et al. 2019) material as well as spacecraft measurements in the  $3\text{-}\mu\text{m}$  range of the Moon (Li & Milliken 2016) and Mars (Milliken 2006) indicate a downturn of the spectrum at typical wavelengths of  $2.6\text{--}2.7 \mu\text{m}$ , whereas in the spectra in Fig. 2b the downturn occurs near  $2.5 \mu\text{m}$ . This effect may be due to a slight overestimation of the surface temperature by the method used. Due to the negligible difference in effective temperature between the bright structure and the surrounding surface, the difference in  $3\text{-}\mu\text{m}$  band depth would hardly be influenced by a slight general systematic overestimation of the surface temperature anyway. Further, the effective temperature used for thermal emission removal is slightly lower inside the structure than outside of it, whereas the  $3\text{-}\mu\text{m}$  band is significantly stronger inside

than outside. This suggests clearly that the observed increased 3- $\mu\text{m}$  band depth inside the structure is real.

The 3- $\mu\text{m}$  band depth was computed similar to previous works (Wöhler et al. 2017b; Grumpe et al. 2019) but with adjusted wavelength ranges. First, we fitted a linear continuum  $c(\lambda)$  to the reflectance spectrum  $R(\lambda)$  across the wavelength range 2.258–2.497  $\mu\text{m}$  and extrapolated it up to 2.936  $\mu\text{m}$  (Fig. 2b). The wavelengths of the fitting interval are shorter than those used by Wöhler et al. (2017b) because of the downturn of the spectra at exceptionally short wavelengths. The integrated 3- $\mu\text{m}$  band depth IBD3 is then given by

$$\text{IBD3} = 100 \times \left[ \int_{\lambda_{\min}}^{\lambda_{\max}} \left( 1 - \frac{R(\lambda)}{c(\lambda)} \right) d\lambda \right] / [\lambda_{\max} - \lambda_{\min}], \quad (1)$$

with  $\lambda_{\min} = 2.537 \mu\text{m}$  and  $\lambda_{\max} = 2.936 \mu\text{m}$ . This quantity corresponds to the mean relative absorption in percent across the interval  $[\lambda_{\min}, \lambda_{\max}]$ .

### 3. Results and discussion

The two available  $M^3$  images M3G20090720T090521 and M3G20090623T012541 of this structure were acquired at local times of 10:00 and 11:45, respectively, corresponding to the midday range in the global study by Wöhler et al. (2017b). The average 3- $\mu\text{m}$  band depth is shown in Fig. 1c. The bright structure between Dufay and Dufay X is the only localized positive 3- $\mu\text{m}$  band depth anomaly of this kind which we found on the Moon after a rigorous search of the  $M^3$ -derived global 3- $\mu\text{m}$  band depth data set of Wöhler et al. (2017b). This anomaly is characterized by an excess in 3- $\mu\text{m}$  band depth of about 30% at midday relative to the surrounding highland surface (Fig. 1), however it is by far not the brightest surface area in the farside highlands. Highland material that is similarly bright does not show positive 3- $\mu\text{m}$  band depth anomalies (see, e.g., the small fresh highland craters in Fig. 1 or the ray systems of large highland craters in the global 3- $\mu\text{m}$  band depth maps by Wöhler et al. (2017b) (see also Fig. A.2). Unfortunately, no  $M^3$  data acquired in the early morning or afternoon are available for this area, while the 3- $\mu\text{m}$  band depth maps acquired at 10:00 and 11:45 are nearly identical. Therefore, the time-of-day-dependent behavior of the 3- $\mu\text{m}$  band depth at the location of the bright structure cannot be assessed based on the available data.

The map of the estimated effective temperature (see also Sect. 2) shown in Fig. 1d indicates that at 11:45 the temperature difference between the bright structure and the surrounding darker surface is below 2 K. This is consistent with the weak dependence (for dark surfaces like that of the Moon) of the surface temperature on the directional-hemispherical surface albedo  $A_{\text{dh}}$  proportional to  $(1 - A_{\text{dh}})^{1/4}$  (Shkuratov et al. 2011). Furthermore, the region of slightly reduced temperature in Fig. 1d only roughly corresponds to the bright structure and is smaller. The increased 3- $\mu\text{m}$  band depth inside the bright structure is therefore most likely not an artifact of the technique used for thermal emission removal.

The global  $M^3$  OH/H<sub>2</sub>O maps by Wöhler et al. (2017b) indicate that in the equatorial lunar highlands the 3- $\mu\text{m}$  band depth differs by less than about 10% between morning and midday or between midday and afternoon. In contrast, recent modeling by Grumpe et al. (2019) has shown that near the equator in the lunar highlands the time-of-day-dependent OH component always decreases to zero at midday due to diffusive loss and photolysis for all examined settings of physical parameters. This finding is confirmed by the model of Farrell et al. (2017),

which predicts H column densities on the surface at low latitudes to be about 10–100 times lower at midday than in the morning and afternoon. This indicates that the excess 3- $\mu\text{m}$  band depth observed in the bright structure at midday is indeed due to a strongly bounded OH/H<sub>2</sub>O component. Hence, one might assume a strongly bounded OH/H<sub>2</sub>O component (e.g., Bandfield et al. 2016) that does not undergo diffusive loss and photolysis and together with the time-of-day-dependent component generates the observed 3- $\mu\text{m}$  band depth behavior (Wöhler et al. 2017b; Grumpe et al. 2019). This strongly bounded OH/H<sub>2</sub>O component may be of endogenous origin (Pieters et al. 2009b), or it might consist of solar-wind-induced OH/H<sub>2</sub>O diffused into binding states in the surface mineral with energies high enough to prevent diffusive loss and photolysis for the duration of a lunar day (Grumpe et al. 2019).

The low soil maturity of the structure is clearly apparent in Fig. 2a showing the optical maturity (OMAT) parameter as given by Lucey et al. (2000) based on Clementine UV/VIS data (Eliason et al. 1999; Hare et al. 2008), and is also indicated by the reduced spectral slope (Hapke 2001) in comparison to the surrounding surface (Fig. 2b). This indicates a younger age than the surrounding surface (due to its location off the magnetic anomaly at Dufay X, magnetic shielding at the location of the bright structure is likely to be absent). The spectra of the structure and the surrounding surface are both typical of anorthositic highland material of very low Fe and Ti content, as they do not show mafic absorption bands near 1  $\mu\text{m}$  and 2  $\mu\text{m}$ . This indicates that there is no perceivable difference in composition between the bright structure and the surrounding surface. Recent simulations based on Mie modeling predict that space-weathering by submicroscopic iron decreases the 3- $\mu\text{m}$  band depth only by a negligible amount (Wohlfarth et al. 2019), which is confirmed by the observation that immature areas such as bright crater rays do not show up as 3- $\mu\text{m}$  band depth anomalies in the global maps of Wöhler et al. (2017b); see also Fig. A.2. Hence, the observed excess in 3- $\mu\text{m}$  band depth cannot be explained by low soil maturity.

All in all, the bright structure near Dufay is of general importance for the understanding of lunar OH/H<sub>2</sub>O: in comparison to global OH/H<sub>2</sub>O data (Wöhler et al. 2017b, Fig. A.2), our observations indicate that the lunar surface near the equator can accumulate OH/H<sub>2</sub>O in higher concentrations than in the illuminated polar highlands despite the high equatorial midday temperatures exceeding 380 K (Fig. 1d). This behavior is in contrast to the common assumption that OH/H<sub>2</sub>O builds up more easily in cool regolith material especially at high latitudes (e.g., Starukhina 2001; Sunshine et al. 2009; Farrell et al. 2017).

Based on the available data, we suggest that the pronounced 3- $\mu\text{m}$  band at midday exhibited by the bright structure near Dufay is not due to its high albedo and low maturity alone but is also due to the occurrence of a surface alteration (of so far unknown nature) that strongly increased the ability of the surface material to adsorb hydrogen from the solar wind and form a OH/H<sub>2</sub>O component that is stable against destruction processes such as diffusive loss and photolysis. An alternative and admittedly speculative interpretation is the formation by recent infall of a thin layer of meteoritic or cometary material of high OH/H<sub>2</sub>O content which is now detectable by its pronounced 3- $\mu\text{m}$  band. Figure 1b shows that none of the craters on the bright structure appear as a dark halo impact crater that excavated dark material from depth. It is therefore possible that the layer of bright material is thicker than the excavation depth of the largest (~2.5 km diameter) craters on it, which can be considered unlikely though, due to the absence of dark halo impact craters even in the (supposedly thinnest) outermost parts of the

structure. It is more plausible that the layer of bright material is thin and formed at recent times, having covered the underlying cratered terrain after the formation of all visible craters.

In the case of a very low impact speed of about  $5 \text{ km s}^{-1}$ , the impact of meteoritic material will not lead to the production of impact vapor and melt (Cintala 1992). For this reason we expect that defects in the crystal grid of material in the vicinity of low-speed impact events survive the impact. These defects can trap part of the impact-produced volatiles released to the exosphere in binding states with relatively high activation energies significantly exceeding 1 eV; according to the physical parameters of Grumpe et al. (2019) and assuming a surface temperature of  $T = 400 \text{ K}$ , the lifetime of such molecules against thermal evaporation will exceed  $\sim 10^4$  years if the activation energy is higher than 1.4 eV. This scenario is realistic because there exist binding states of OH/H<sub>2</sub>O in silica with activation energies of up to  $\sim 2 \text{ eV}$  (Zhuravlev 2000). Alternatively, the OH/H<sub>2</sub>O might have been contained in the meteoritic material in the form of hydrated minerals, where they would have survived higher impact speeds than pure water ice without being released from their parent minerals. In both cases, the OH/H<sub>2</sub>O must be located at a depth inaccessible to ultraviolet photons, which prevents photolysis, but accessible to NIR photons (see also Grumpe et al. 2019). This mechanism would also be an explanation for the fact that only one such structure can be observed on the Moon, because similar older structures would become invisible to NIR spectroscopy due to gardening of the regolith.

It can be expected that the impact of meteoritic or cometary material changes the structure of the upper regolith layer with respect to, for example, regolith porosity, roughness, and light scattering behavior, even in the case of small impacting grains. Therefore, the presented hypothesis of the origin of the bright structure near Dufay may be supported by future photometric observations of the region across a broad range of phase angles. For small phase angles, such measurements would provide information about the regolith porosity (Hapke 2002), while at intermediate phase angles variations in the surface roughness and the slope of the phase function might be revealed, for example, by the technique of phase ratio imaging (Shkuratov et al. 2011).

Furthermore, observations of possible time-of-day-dependent variations of the 3- $\mu\text{m}$  band depth and shape inside the structure, using, for example, the upcoming Chandrayaan-2 imaging spectrometer IIRS (Annadurai 2017), are highly recommendable. The spectral range of IIRS of 0.8–5  $\mu\text{m}$  (AMOS<sup>1</sup>) will provide complete coverage of the 3  $\mu\text{m}$  band, allowing for the analysis of the time-of-day-dependent band depth and shape as well as possibly the distinction between OH and H<sub>2</sub>O and an estimation of their respective time-of-day-dependent fractions. Such observations would yield insights into the weakly vs. strongly bounded abundances of OH and H<sub>2</sub>O. In particular, if the time-of-day-dependent, weakly bounded OH/H<sub>2</sub>O component inside the structure near Dufay was found to behave similarly to the surrounding surface, indicating that there is only an excess of strongly bounded OH/H<sub>2</sub>O, that observation would support the assumption of a recent infall of meteoritic material rich in OH/H<sub>2</sub>O.

#### 4. Conclusion

We identified a unique bright structure located near the lunar equatorial highland crater Dufay, which is characterized by an

excess in 3- $\mu\text{m}$  absorption band depth of  $\sim 30\%$  at local midday. Its spectral behavior indicates a low soil maturity and a typical feldspathic highland composition with no detectable mafic component, and no compositional difference to the surrounding highland terrain was detected. The structure is unique on the Moon as its 3- $\mu\text{m}$  band is even stronger than in the illuminated polar highlands. The suggested explanation for the observed behavior is a recent low-speed infall of a thin layer of OH/H<sub>2</sub>O-rich meteoritic or cometary material, where the spectrally observed OH/H<sub>2</sub>O is assumed to be bounded in states of relatively high activation energy. We recommend targeted photometric and spectral observations of the structure with new dedicated spacecraft instrumentation in order to gain a more detailed understanding of the physical processes leading to the accumulation of OH/H<sub>2</sub>O in the lunar regolith surface.

*Acknowledgements.* The spacecraft data processed in this study were downloaded from the Planetary Data System (M<sup>3</sup> data: <https://pds-imaging.jpl.nasa.gov/volumes/m3.html>; LRO WAC data: [http://wms.lroc.asu.edu/lroc/view\\_rdr/WAC\\_GLOBAL](http://wms.lroc.asu.edu/lroc/view_rdr/WAC_GLOBAL); Clementine data: [https://astrogeology.usgs.gov/search/map/Moon/Clementine/UVVIS/Lunar-Clementine\\_UVVIS\\_WarpMosaic\\_5Bands\\_200m](https://astrogeology.usgs.gov/search/map/Moon/Clementine/UVVIS/Lunar-Clementine_UVVIS_WarpMosaic_5Bands_200m)). C. W. and A. G. were funded by the Deutsche Forschungsgemeinschaft (DFG, German Research Foundation), project no. 277133575. A. A. B. was partially supported by TU Dortmund University. A. B. and M. B. were supported by the Department of Space, Government of India.

#### References

- Annadurai, M. 2017, in *60th session of the United Nations Committee on Peaceful Exploration of Outer Space, Vienna, Austria*
- Bandfield, J. L., Hayne, P. O., Williams, J.-P., Greenhagen, B. T., & Paige, D. A. 2015, *Icarus*, **248**, 357
- Bandfield, J. L., Edwards, C. S., Poston, M. J., & Klima, R. L. 2016, *Lunar Planet. Sci. Conf.*, **47**, 1594
- Bandfield, J. L., Poston, M. J., Klima, R. L., & Edwards, C. S. 2018, *Nat. Geosci.*, **11**, 173
- Beck, P., Quirico, E., Montes-Hernandez, G., et al. 2010, *Geochim. Cosmochim. Acta*, **74**, 4881
- Bhardwaj, A., Dhanya, M. B., Alok, A., et al. 2015, *Geosci. Lett.*, **2**, 10
- Bhattacharya, S., Saran, S., Dagar, A., et al. 2013, *Curr. Sci.*, **105**, 685
- Cintala, M. J. 1992, *J. Geophys. Res.*, **97**, 947
- Clark, R. N., Pieters, C. M., Green, R. O., Boardman, J. W., & Petro, N. E. 2011, *J. Geophys. Res.*, **116**, E00G16
- Davidsson, B. J. R., Rickman, H., Bandfield, J. L., et al. 2015, *Icarus*, **252**, 1
- Denevi, B. W., Robinson, M. S., Boyd, A. K., Blewett, D. T., & Klima, R. L. 2016, *Icarus*, **273**, 53
- Dyar, M., Hibbitts, C., & Orlando, T. 2010, *Icarus*, **208**, 425
- Eliason, E., Isbell, C., Lee, E., et al. 1999, *Mission to the Moon: The Clementine UVVIS Global Lunar Mosaic*, PDS Volumes USA\_NASA\_PDS\_CL\_4001 through 4078, USGS, Distr. on CDROM by Planetary Data System
- Farrell, W. M., Hurley, D. M., & Zimmerman, M. I. 2015, *Icarus*, **255**, 116
- Farrell, W. M., Hurley, D. M., Esposito, V. J., McLain, J. L., & Zimmerman, M. I. 2017, *J. Geophys. Res. Planets*, **122**, 269
- Goswami, J. N., & Annadurai, M. 2009, *Curr. Sci.*, **96**, 486
- Grumpe, A., & Wöhler, C. 2014, *ISPRS J. Photogramm. Remote Sens.*, **94**, 37
- Grumpe, A., Wöhler, C., Berezhnoy, A. A., & Shevchenko, V. V. 2017, in *Proc. European Lunar Symposium, Münster, Germany*
- Grumpe, A., Wöhler, C., Berezhnoy, A. A., & Shevchenko, V. V. 2019, *Icarus*, **321**, 486
- Hapke, B. 1984, *Icarus*, **59**, 41
- Hapke, B. 2001, *J. Geophys. Res.*, **106**, 10039
- Hapke, B. 2002, *Icarus*, **157**, 523
- Hare, T. M., Archinal, B. A., Becker, T. L., et al. 2008, *Lunar Planet. Sci. Conf.*, **39**, 2337
- Isaacson, P., Besse, S., Petro, N., Nettles, J., & Team, M. 2011, *M<sup>3</sup> Overview and Working with M<sup>3</sup> Data* [http://pds-imaging.jpl.nasa.gov/documentation/Isaacson\\_M3\\_Workshop\\_Final.pdf](http://pds-imaging.jpl.nasa.gov/documentation/Isaacson_M3_Workshop_Final.pdf)
- Isaacson, P. J., Petro, N. E., Pieters, C. M., et al. 2013, *J. Geophys. Res. Planets*, **118**, 369
- Kramer, G. Y., Besse, S., Dhingra, D., et al. 2011, *J. Geophys. Res. Planets*, **116**, E00G18

<sup>1</sup> CHANDRAYAAN-2 Spectrometer for IIRS, <https://www.amos.be/project/chandrayaan-2>, accessed July 12, 2019.

- Li, S., & Milliken, R. E. 2016, *J. Geophys. Res.*, **121**, 2282
- Li, S., & Milliken, R. E. 2017, *Sci. Adv.*, **3**, e1701471
- Lucey, P. G., Blewett, D. T., Taylor, G. J., & Hawke, B. R. 2000, *J. Geophys. Res.*, **105**, 20377
- Milliken, E. E. 2006, PhD Thesis, Brown University, USA
- Pieters, C. M., Boardman, J., Buratti, B., et al. 2009a, *Curr. Sci.*, **96**, 500
- Pieters, C. M., Goswami, J. N., Clark, R. N., et al. 2009b, *Science*, **326**, 568
- Sato, H., Robinson, M. S., Hapke, B., Denevi, B. W., & Boyd, A. K. 2014, *J. Geophys. Res. Planets*, **119**, 1775
- Scholten, F., Oberst, J., Matz, K.-D., et al. 2012, *J. Geophys. Res.*, **117**, E00H17
- Shkuratov, Y., Kaydash, V., Korokhin, V., et al. 2011, *Planet. Space Sci.*, **59**, 1326
- Speyerer, E. J., Wagner, R. V., Robinson, M. S., et al. 2016, *Space Sci. Rev.*, **200**, 357
- Starukhina, L. V. 2001, *J. Geophys. Res.*, **106**, 14701
- Sunshine, J. M., Farnham, T. L., Feaga, L. M., et al. 2009, *Science*, **326**, 565
- Takir, D., Stockstill-Cahill, K. R., Hibbitts, C. A., & Nakauchi, Y. 2019, *Icarus*, **333**, 243
- Tsunakawa, H., Takahashi, F., Shimizu, H., Shibuya, H., & Matsushima, M. 2015, *J. Geophys. Res. Planets*, **120**, 1160
- Warell, J. 2004, *Icarus*, **167**, 271
- Wöhler, C., Grumpe, A., Berezhnoy, A., Bhatt, M. U., & Mall, U. 2014, *Icarus*, **235**, 86
- Wöhler, C., Grumpe, A., Berezhnoy, A. A., et al. 2017a, *Icarus*, **285**, 118
- Wöhler, C., Grumpe, A., Berezhnoy, A. A., & Shevchenko, V. V. 2017b, *Sci. Adv.*, **3**, E1701286
- Wohlfarth, K. S., Wöhler, C., & Grumpe, A. 2019, *Astron. J.*, **158**, 80
- Zhuravlev, L. T. 2000, *Coll. Surf. A Physicochem. Eng. Asp.*, **173**, 1

Appendix A: Supplementary material

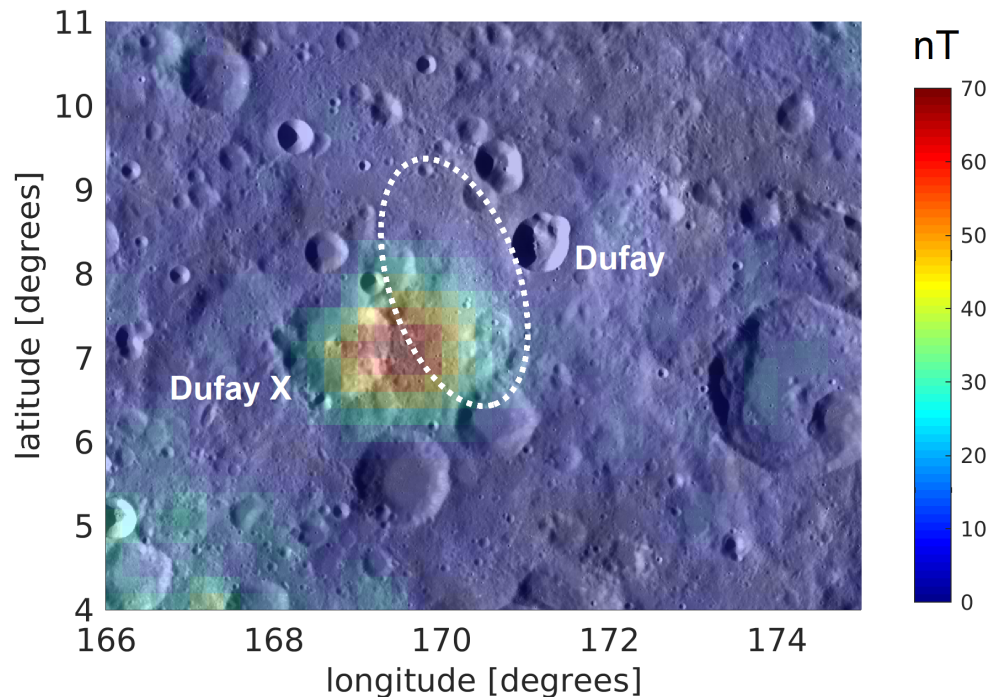


**Fig. A.1.** Magnetic flux density on the ground in nT in the region around the craters Dufay and Dufay X according to [Tsunakawa et al. \(2015\)](#), overlaid on LRO WAC ([Speyerer et al. 2016](#); [Sato et al. 2014](#)).

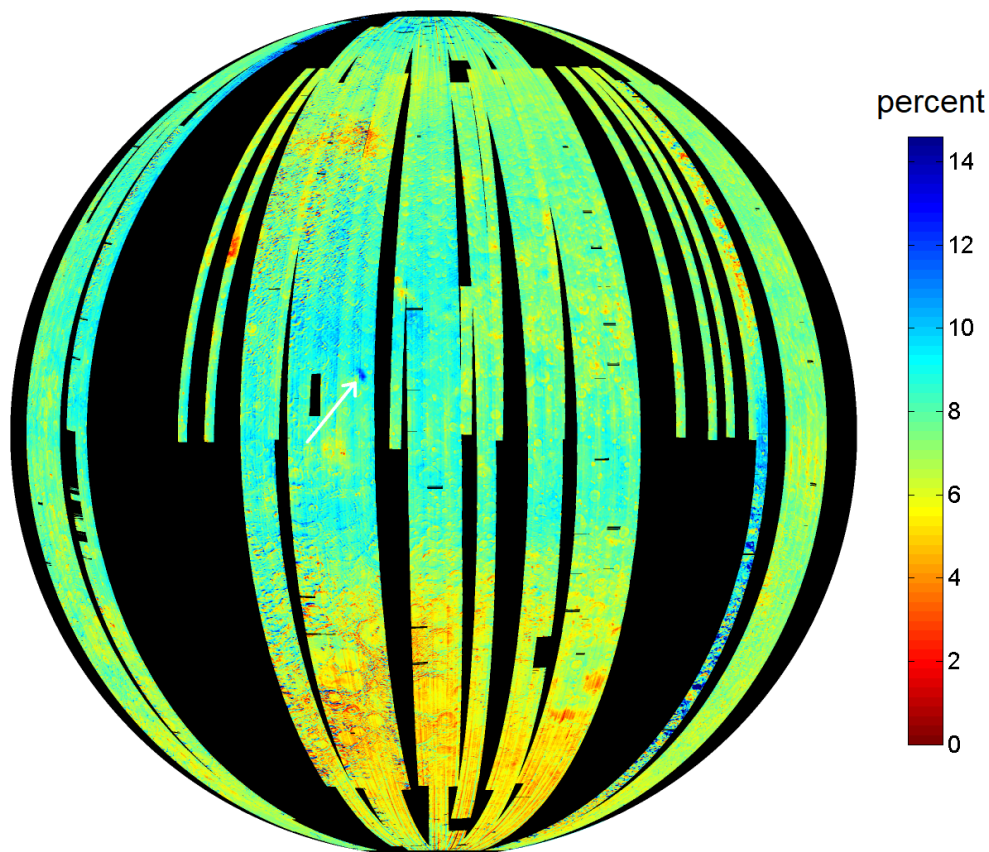


**Fig. A.2.**  $M^3$ -based Map of the 3- $\mu\text{m}$  band depth at midday (10:00–12:00 local time) on the lunar farside, orthographic projection, central meridian  $180^\circ$  (from [Wöhler et al. 2017b](#)). The bright structure, which appears very small at global scale, is marked by a white arrow.